ceramics

MDPI

Article

An Investigation of the Microstructure and Wear Resistance of Laser Clad 316 Stainless Steel/TiC Coatings Containing Different LaB_6 Contents

Dongdong Zhang [1,*], Haozhe Li [1], Yu Liu [1,2], Jingyu Jiang [1] and Yali Gao [1]

[1] School of Mechanical Engineering, Northeast Electric Power University, No. 169 Changchun Road, Chuanying District, Jilin 132012, China; 15584082910@163.com (H.L.); yuliu@neepu.edu.cn (Y.L.); 17891048717@163.com (J.J.); dehuigyl@126.com (Y.G.)

[2] International Shipping Research Institute, Jiujiang Vocational University of Science and Technology, Gongqing 332020, China

* Correspondence: zhangdongdong@neepu.edu.cn

Abstract

In this paper, 316 stainless steel/TiC coatings with different LaB_6 contents (0%, 2%, 4%, 6%) were prepared on the surface of 45 steel by laser cladding technology. The effects of the LaB_6 content on the phase composition, microstructure, microhardness, and wear resistance of the coatings were studied. The results show that without the LaB_6 addition, the coating is composed of Austenite and TiC phases, with defects such as pores and cracks, and the microstructure is mainly equiaxed grains. With the addition of LaB_6, Fe-Cr phases are formed in the coating, and the microstructure transforms into columnar grains and dendritic grains. The grains are first refined and then coarsened, among which the coating with 4% LaB_6 (C4) has the smallest grain size. The experimental results indicate that the microhardness of the coatings first increases and then decreases with the increase in the LaB_6 content, and the C4 coating has the highest microhardness (594$HV_{0.2}$). The wear rate shows the same variation trend. The C4 coating has the lowest wear rate and the best wear resistance. This is attributed to the synergistic effect of the fine grain strengthening and TiC particle dispersion strengthening.

Keywords: laser cladding; coating; LaB_6 modification; wear resistance

Academic Editors: Gilbert Fantozzi and Vincent Garnier

Received: 1 August 2025
Revised: 15 September 2025
Accepted: 23 September 2025
Published: 26 September 2025

Citation: Zhang, D.; Li, H.; Liu, Y.; Jiang, J.; Gao, Y. An Investigation of the Microstructure and Wear Resistance of Laser Clad 316 Stainless Steel/TiC Coatings Containing Different LaB_6 Contents. *Ceramics* **2025**, *8*, 121. https://doi.org/10.3390/ceramics8040121

1. Introduction

As a commonly used medium for carbon quenched and tempered steel, 45 steel is widely used in the manufacture of various components in mining machinery due to its good mechanical properties [1–3]. In the field of mining machinery, 45 steel is mainly used in shaft components (such as drive shafts and mandrels), as well as gears, racks, etc. [4]. However, in the actual working environment of mining machinery, there are hard rock particles, ores, and frequent impact loads, which lead to the main failure mode of 45 steel parts occurring on the surface [5]. This will lead to a gradual decline in the performance of 45 steel surfaces, affecting the normal operation of machinery and production efficiency.

Regarding the wear problem of 45 steel components in the mining machinery operation environment, laser cladding technology provides an effective solution to enhance their surface wear resistance [6,7]. High-energy laser beams are used to simultaneously melt specific materials onto the surface of the 45 steel substrate during the laser cladding process, forming a rapidly solidified molten pool [8,9]. Subsequently, the molten pool rapidly

solidifies on the surface of the substrate, forming a coating that is metallurgically bonded to the 45 steel substrate [10]. Titanium carbide (TiC) exhibits characteristics of a high melting point and exceptional hardness, making it a good choice for preparing wear-resistant coatings [11–13]. Bu et al. [14] prepared Al + TiC coatings on the surface of AZ63-Er. When the mass ratio of Al:TiC was 2:1, the hardness of the coating was approximately 3.94 times that of the AZ63-Er alloy substrate. Xu et al. [15] used laser cladding technology to fabricate a 90 wt.% TiC + 10 wt.% Ni60 coating on the surface of Ti6Al4V. The test results showed that the coating exhibited better wear resistance at a low scanning speed. However, the thermophysical properties of TiC ceramic materials are different from those of metals. This discrepancy may result in the formation of defects such as pores or cracks within the coating during the laser cladding process [16,17].

Previous studies have shown that adding rare earth elements to coatings can produce the following effects: the refinement of the microstructure, a reduction in the grain size, the homogenization of coating elements, and the improvement of tribological and mechanical properties. The absorption of rare earth elements in the laser cladding material system may reduce the dilution rate, improve the toughness of the coating, and decrease the cracking tendency [18,19]. Meng et al. [20] used laser cladding technology to fabricate three micro-nanostructure Al_2O_3-NiCr coatings containing nano-sized rare earth oxides (CeO_2, La_2O_3, and Sm_2O_3) on the surface of H13 steel. They found that the microstructure of the coatings with added nano-sized rare earth oxides was refined. Additionally, the influence of nano-Sm_2O_3 oxide on the alloy structure and wear resistance was superior to that of CeO_2 and La_2O_3. Mohammed et al. [21] laser cladded 1% and 2% La_2O_3 and 1% and 2% CeO_2 on the surface of ASTM A36 steel. They found that the 40% Ni-60% WC coating had a significantly higher microhardness compared to the substrate. The addition of La_2O_3 and CeO_2 further enhanced the hardness. Compared to adding CeO_2, the addition of La_2O_3 led to a more significant increase in hardness. Li et al. [22] prepared FeCoNiCrMo high entropy alloy (HEA) coatings with different La_2O_3 contents on the surface of 65 Mn steel. The research results showed that La_2O_3 can reduce the incidence of pores in the HEA coating and effectively improve the hardness and wear resistance of the coating. However, there are adverse effects on the hardness and wear resistance of the coating when excessive La_2O_3 is added. The coating exhibits the lowest wear loss and the best wear resistance when 8% La_2O_3 is added.

However, there are few reports on LaB_6-reinforced 316 stainless steel/TiC composites. In this study, different contents of LaB_6-reinforced 316 stainless steel/TiC coatings were prepared on the surface of 45 steel by laser cladding. The phase composition, microstructure, microhardness, and wear resistance of the coating with different contents of LaB_6 were analyzed. This research provides a certain theoretical basis for optimizing the content of rare earth borides.

2. Materials and Methods

2.1. Sample Preparation

In this study, 45 steel (Mingshang Special Steel Co., Ltd., Wuxi, China) was selected as the substrate for laser cladding. The sample size was 50 mm × 30 mm × 10 mm, and the chemical composition is shown in Table 1. For the present study, commercially available 316 stainless steel powder of micron size (supplied by Xingtai Xinnai Metal Materials Co., Ltd., Xingtai, China) with a stated purity of 99.9% and an average particle size of 45 μm was selected as the powder feedstock. Titanium carbide (TiC) and LaB_6, also obtained from Xingtai Xinnai Metal Materials Co., Ltd., Xingtai, China, was used as the reinforcement. The purity of TiC and LaB_6 is 99.9%, with an average particle size of approximately 45 μm. The chemical composition of 316 stainless steel spherical powder is shown in Table 2.

Table 1. Chemical composition of 45 steel (wt.%).

Element	C	Si	Mn	Ni	Cr	Cu	Fe
Component	0.42~0.50	0.17~0.37	0.50~0.80	≤0.30	≤0.25	≤0.25	Bal.

Table 2. Chemical composition of 316 stainless steel (wt.%).

Element	C	Si	Mn	Mo	Ni	Cr	Fe
Component	0.06	0.92	1.51	2.55	13.23	17.24	Bal.

Before the experiment, the surface of 45 steel was polished with 150 # sandpaper to remove the oxide layer, cleaned with acetone to remove the oil stain, and then dried in an argon environment for half an hour. The complete composition of the different samples is provided in Table 3. Among them, Hybrid 316 stainless steel + TiC composites were synthesized by fixing the content of TiC at 10 wt.% for all compositions, while the amount of LaB_6 was varied between 0 and 6 wt.% in steps of 2 wt.%.

The equipment used in the laser cladding experiment is a CO_2 laser processing system (DL-HL-T2000B, Shenyang Continental Laser Complete Equipment Co., Ltd., Shenyang, China), with a maximum power of 2000 W and a wavelength of 10.6 μm. Preset powder method was adopted in this experiment, with the powder placement height being 1 mm ± 0.1 mm. In this experiment, the laser power was 1200 W, the scanning speed was 480 mm/min, the spot diameter was 3 mm, and the overlap rate was 30%. Argon gas was used as the protective gas during the preparation of the coating, and the flow rate was 6 L/min. The samples prepared by laser cladding from the powders with 0, 2, 4, and 6 wt.% LaB_6 were indicated as C0, C2, C4, and C6, respectively. Figure 1 shows the principle diagram of laser cladding.

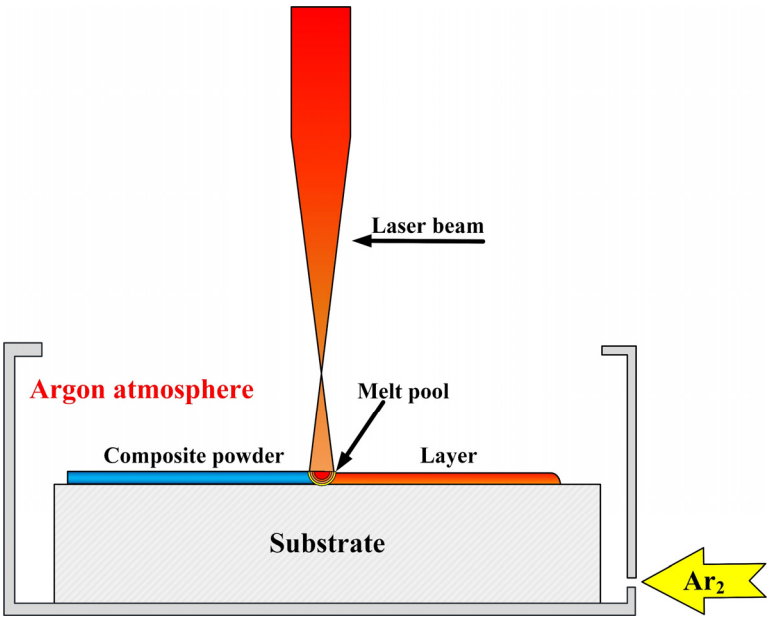

Figure 1. Schematic representation of the fabrication process for 316 stainless steel + TiC composites by laser cladding.

Table 3. Composition details of synthesized 316 stainless steel + TiC composites containing fixed 10 wt.% TiC and varying LaB_6 content (0–6 wt.%).

Sample	Mixed Powders (wt.%)	LaB_6 Powder (wt.%)
C0	100	0
C2	98	2
C4	96	4
C6	94	6

2.2. Characterizations of the Samples

The wire-cutting machine was used to take the size of 10 mm × 10 mm × 10 mm. Four kinds of water abrasive paper (180 #, 600 #, 1200 #, 2000 #) were used to grind and polish the cross-section of the substrate. After polishing, the sample was chemically etched with aqua regia etching solution (HNO_3:HCl = 3:1) until the surface of the sample was discolored. After the corrosion process is completed, the sample should be cleaned and dried. The microstructure of the samples was observed using scanning electron microscopy (SEM) (Zeiss eSigma300, Oberkochen, Germany), and the chemical composition was analyzed using an energy dispersive spectrometer (EDS) attached to the SEM. The phase analysis of the cladding layer was conducted using X-ray diffraction instrument (TD-3500, Tongda Technology Co., Ltd., Dandong, China). CuKα was selected for the experiment, and the scanning mode was continuous scanning, with an angle scanning range of 20–90°.

The microhardness distribution of the cladding layer section was measured by Vickers microhardness tester (HXD-1000TMC/LCD, Wuxi Metes Precision Technology Co., Ltd., Wuxi, China) under the load condition of 200 gf and load holding time of 10 s. One point was selected every 0.1 μm in the horizontal direction for three times. The average microhardness value obtained from the three measurements at this point was calculated as the microhardness value of this point. The tribological properties of the cladding layer were tested by a fatigue reciprocating friction and wear tester (MGW-02, Jinan Yihua Frictional Testing Technology Co., Ltd., Jinan, China). During the test, the surface of the coating was polished. The friction mode used was reciprocating dry friction. The applied load was 30 N, the sliding distance was 3 mm, and the friction time was 30 min. The Si_3N_4 grinding ball with a diameter of 5 mm was selected for the grinding ball. After the wear test was completed, the wear morphology of the sample was observed using SEM and EDS, and the wear volume was estimated. The wear rate was also calculated.

3. Results and Discussion

3.1. Phase Analysis

The XRD diffraction results of the C0~C6 coatings are shown in Figure 2. The phase of the coating is composed of Austenite and TiC when LaB_6 is not added. With the increase in the LaB_6 content, the diffraction intensity of the Austenite phase continuously decreases, concurrently with the formation and progressive enhancement of the Fe-Cr phase. This indicates that the addition of LaB_6 promoted the formation of the Fe-Cr phase. This is due to the fact that the XRD diffraction intensity is positively correlated with the volume fraction of the corresponding phase. When the volume fraction of the Fe-Cr phase increases with the increase in the LaB_6 content, the volume fraction of the Austenite phase decreases accordingly, directly resulting in the continuous weakening of its diffraction peak intensity. In addition, due to the low addition amount of LaB_6 and the volume fraction of the phase being below the recognition threshold of the XRD instrument, the LaB_6 phase was not detected.

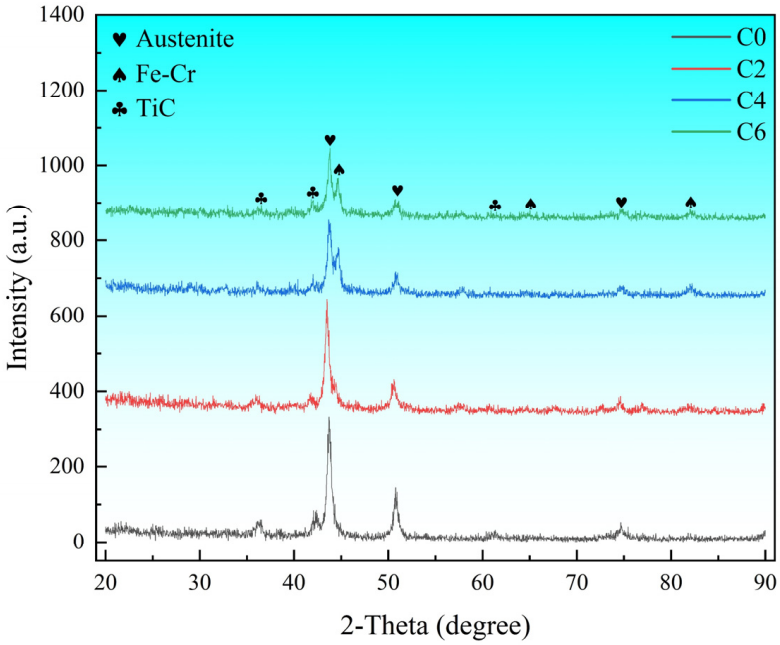

Figure 2. X-ray diffraction pattern of the C0 to C6 coatings.

3.2. Macroscopic Morphology and Microstructure Analysis

Figure 3 shows the macroscopic morphology of the C0 to C6 coatings. As can be seen from Figure 3a, pores and cracks exist on the surface of the C0 coating. This is due to the difference in the thermal expansion coefficients between the TiC particles and the 316 stainless steel. During the laser cladding process, the mismatch in the thermal expansion and contraction between the TiC particles in the molten pool and the surrounding molten 316 material leads to local stress concentration, resulting in the formation of pores and cracks. No cracks were observed in Figure 3b–d, but a few pores were observed in Figure 3b. This is due to the addition of LaB_6, which improves the stress concentration phenomenon of the coating and reduces the generation of pores and cracks. In addition, due to the relatively large atomic radius of La (195 pm) as a surface-active element, La is prone to distribute on the grain boundaries of the coating. When the grains grow, the La atoms and compounds on the grain boundaries exert a dragging effect on the movement of the grain boundaries, thereby inhibiting the growth of the grains [23] and achieving the effect of refining the grains. According to the principle of fine grain strengthening, the grain boundaries can act as a "stress transmission barrier", dispersing the stress originally concentrated at the interface of large grains to more fine grain boundaries, thereby reducing the local stress peak and alleviating the phenomenon of the stress concentration. At the same time, the plastic deformation ability of the fine-grain structure is stronger, which can absorb part of the solidification stress through minor deformation, further reducing the driving force for crack initiation. In addition, the coating thickness shows a gradually increasing trend with the increase in the LaB_6 content. Among them, the C0 coating has the smallest thickness. This is due to the fact that the radius of the La element is relatively large, which reduces the element diffusion between the coating and the substrate. As the content of LaB_6 increases continuously, the degree of the element diffusion also decreases, so the coating thickness keeps increasing.

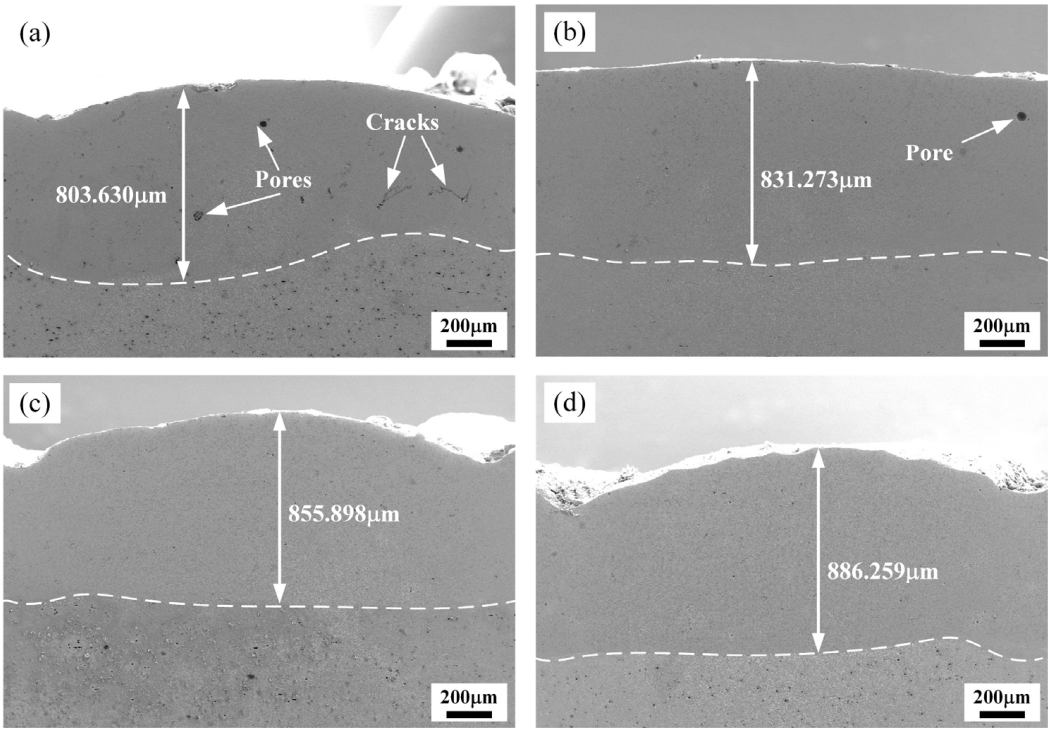

Figure 3. Macroscopic morphology of the C0 to C6 coatings. (**a**) C0; (**b**) C2; (**c**) C4; and (**d**) C6.

The microstructure of the C0 to C6 coatings is shown in Figure 4. It can be seen from Figure 4a that the upper part of the coating without LaB_6 is mainly composed of dense equiaxed crystals, and the bottom is mainly composed of larger equiaxed crystals. In addition, there are also a large number of irregularly shaped block particles distributed within the coating. The coating undergoes a transformation from equiaxed crystals to columnar crystals and dendritic crystals when LaB_6 is added. The size of the grain boundary region within the coating gradually increases, which will lead to a reduction in the lattice distortion, a decrease in the grain boundary impurity concentration, and a reduction in the dislocation density. As a result, the generation of cracks is inhibited. Furthermore, it was observed that the grain size exhibited a trend of initially decreasing and then increasing with the increase in the content of LaB_6. Among them, the C4 coating showed the smallest grain size. This is because that La elements act as heterogeneous nucleation sites, reducing the undercooling of the molten pool and playing a role in fine grain strengthening.

Figure 5 shows the element distribution of the C0 to C6 coatings. Among them, Ti and C elements are enriched in the block particles, so the block particles are TiC phases. As can be seen from Figure 5a, the elements of Fe, Cr, and Ni are uniformly distributed within the C0 coating. Combined with the XRD results, it can be concluded that the regions outside the block particles areas are Austenite phases. From Figure 5b–d, it can be seen that the Cr element precipitates at the grain boundaries when LaB_6 is added, while the Fe element is uniformly distributed in the coating. Combined with the XRD results, it can be observed that the Fe-Cr phase is distributed at the grain boundaries.

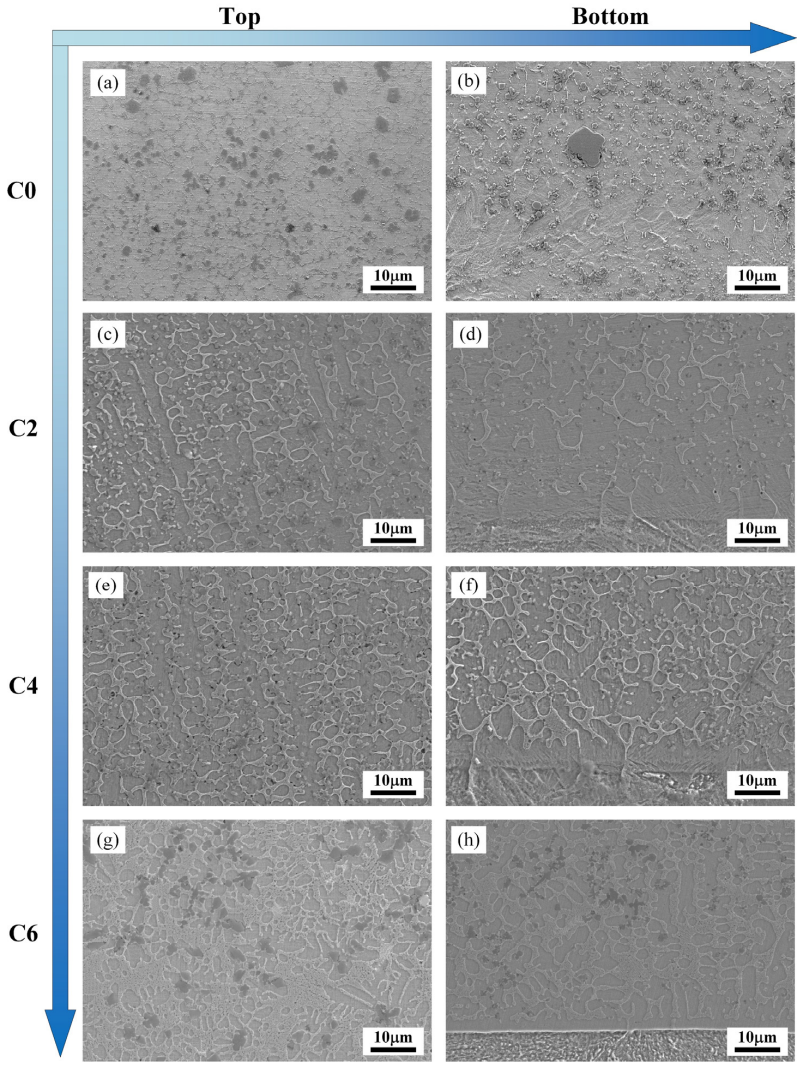

Figure 4. The microstructure of the C0 to C6 coatings. (**a**,**b**) C0; (**c**,**d**) C2; (**e**,**f**) C4; (**g**,**h**) C6.

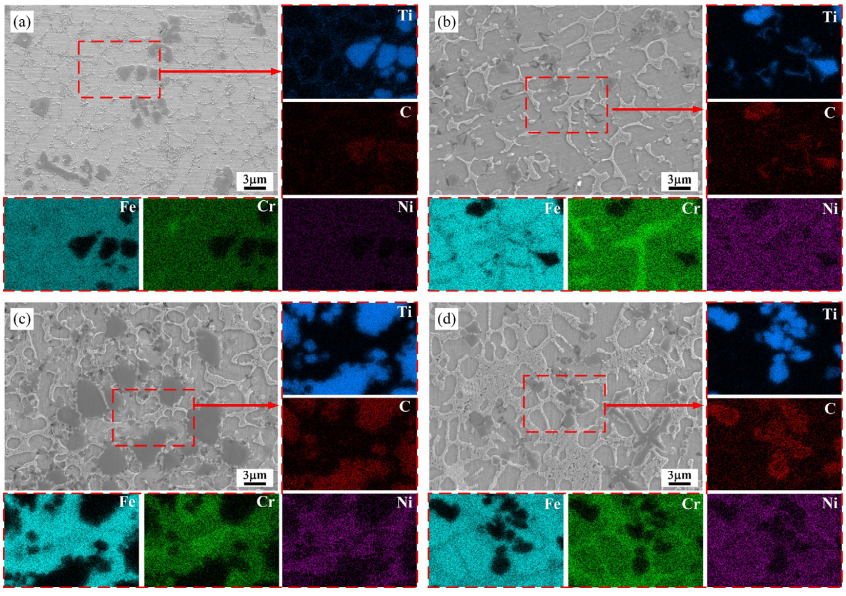

Figure 5. The distribution of elements of the C0 to C6 coatings. (**a**) C0; (**b**) C2; (**c**) C4; (**d**) C6.

3.3. Microhardness Analysis

Figure 6 shows the microhardness distribution of the sample cross-section from the top of the coating to the substrate. As can be seen from Figure 6, compared with sample C0, the microhardness of the coatings of samples C2, C4, and C6 has significantly increased. This is because the C4 coating exhibits the smallest grain size. According to the Hall–Petch formula (Equation (1)) [24], it can be concluded that the microhardness of the coating increases as the grain size decreases, and therefore the fine grain strengthening effect is the most obvious. Furthermore, the TiC particles evenly distributed within the coating play a role in dispersion strengthening. Therefore, the combined effect of the fine grain strengthening caused by the addition of LaB_6 particles and the dispersion strengthening by TiC particles enhanced the microhardness of the composite coating. Figure 6 shows the average microhardness of the C0 to C6 coatings. As the content of LaB_6 in the coating increases, the average microhardness of the coating first rises and then decreases. When the content of LaB_6 is 4%, the microhardness is the highest, at approximately 594 $HV_{0.2}$. When the content of LaB_6 increases to 6%, the microhardness decreases to 527 $HV_{0.2}$. Therefore, an excessive content of LaB_6 will weaken the microhardness of the coating.

$$\sigma_y = \sigma_0 + \frac{k_y}{\sqrt{d}} \quad (1)$$

In this formula, σ_y is the yield strength of the material; σ_0 is the yield strength of the material in the limit of the infinite grain size; k is the Hall–Petch constant, which is a material-specific constant; and d is the average grain size of the material.

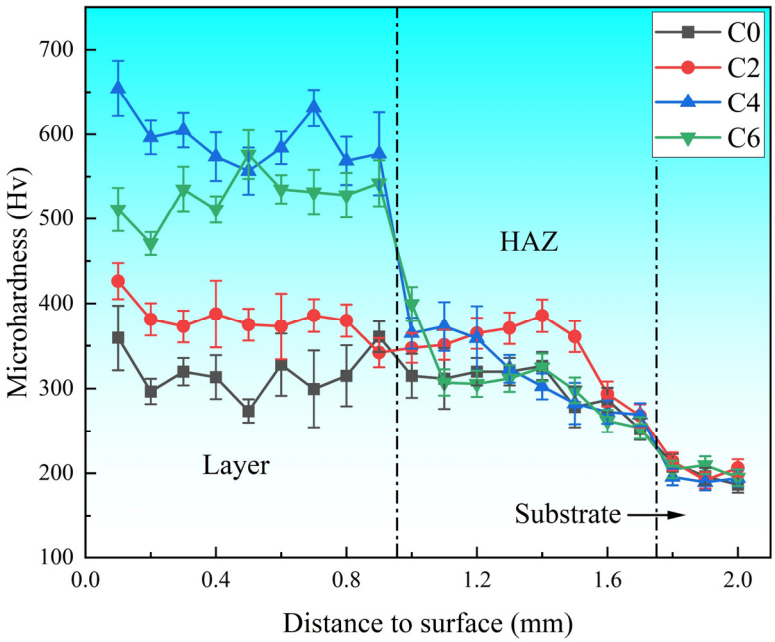

Figure 6. The microhardness distribution of the C0 to C6 coatings.

3.4. Tribological Analysis

The change in the coefficient of friction (COF) with respect to the sliding distance during the wear tests is shown in Figure 7a. During the initial stage of wear (before 200 s), an initial contact occurs between the sample surface and the contact surface, and a state of instability persists. After the initial stage of wear, as the wear progresses, the contact between the sample surface and the grinding balls stabilizes and remains in a stable state until the test is completed. Figure 7b shows the average friction coefficient of the coating. The average friction coefficients of the four coatings do not vary significantly.

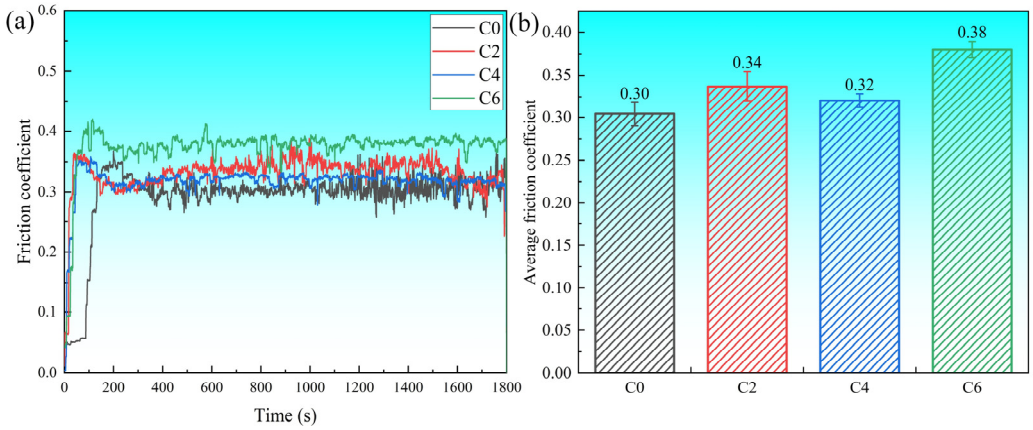

Figure 7. (**a**) A curve showing the variation in the coefficient of friction of the C0 to C6 coatings over time. (**b**) The average friction coefficient of the C0 to C6 coatings.

Figure 8 shows the wear rate of the C0 to C6 coatings. Among them, the C0 coating exhibited the highest wear rate. As the content of LaB_6 increases, the wear rate of C0 to C6 shows a trend of first decreasing and then increasing. The C4 coating exhibited the best wear resistance, which was attributed to the increase in LaB_6 that reduced the grain size and achieved the effect of fine grain strengthening.

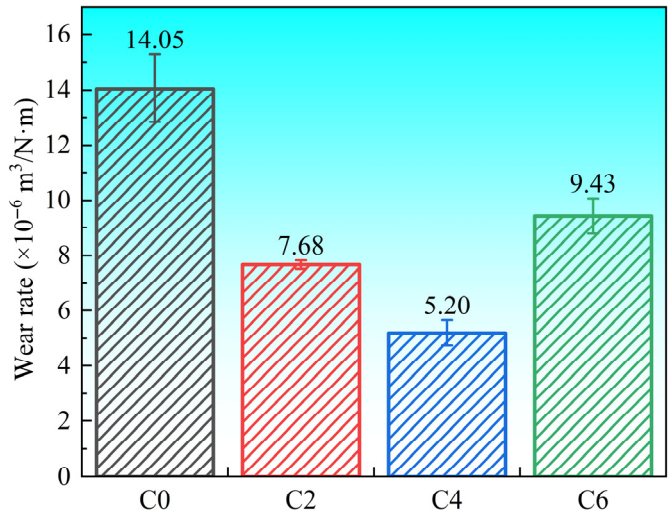

Figure 8. The wear rate of the C0 to C6 coatings.

The wear morphology and element distribution on the C0 to C6 coating surfaces are shown in Figure 9. Oxides are attached to the worn surfaces of C0~C6 coatings. This is because in the wear process, the friction surface between the grinding ball and the coating is not a complete plane contact; in fact, the surfaces of the two convex points make contact with each other. Under the action of the external load, these points make contact and press each other, forming atomic-level metal bond connections. The high temperature generated instantly during the wear process will cause the contact surface to oxidize rapidly and finally form an oxide layer. Except for the C4 coating, spalling pits are also observed on the worn surface. This is because under the action of the external load, after multiple stress cycles, small pieces of material peel off in local areas of the interacting surfaces, forming pitting or pits, which is a typical feature of fatigue wear. The C4 coating has higher hardness and an enhanced ability to resist plastic deformation. Therefore, it prevents the occurrence of spalling during the wear process.

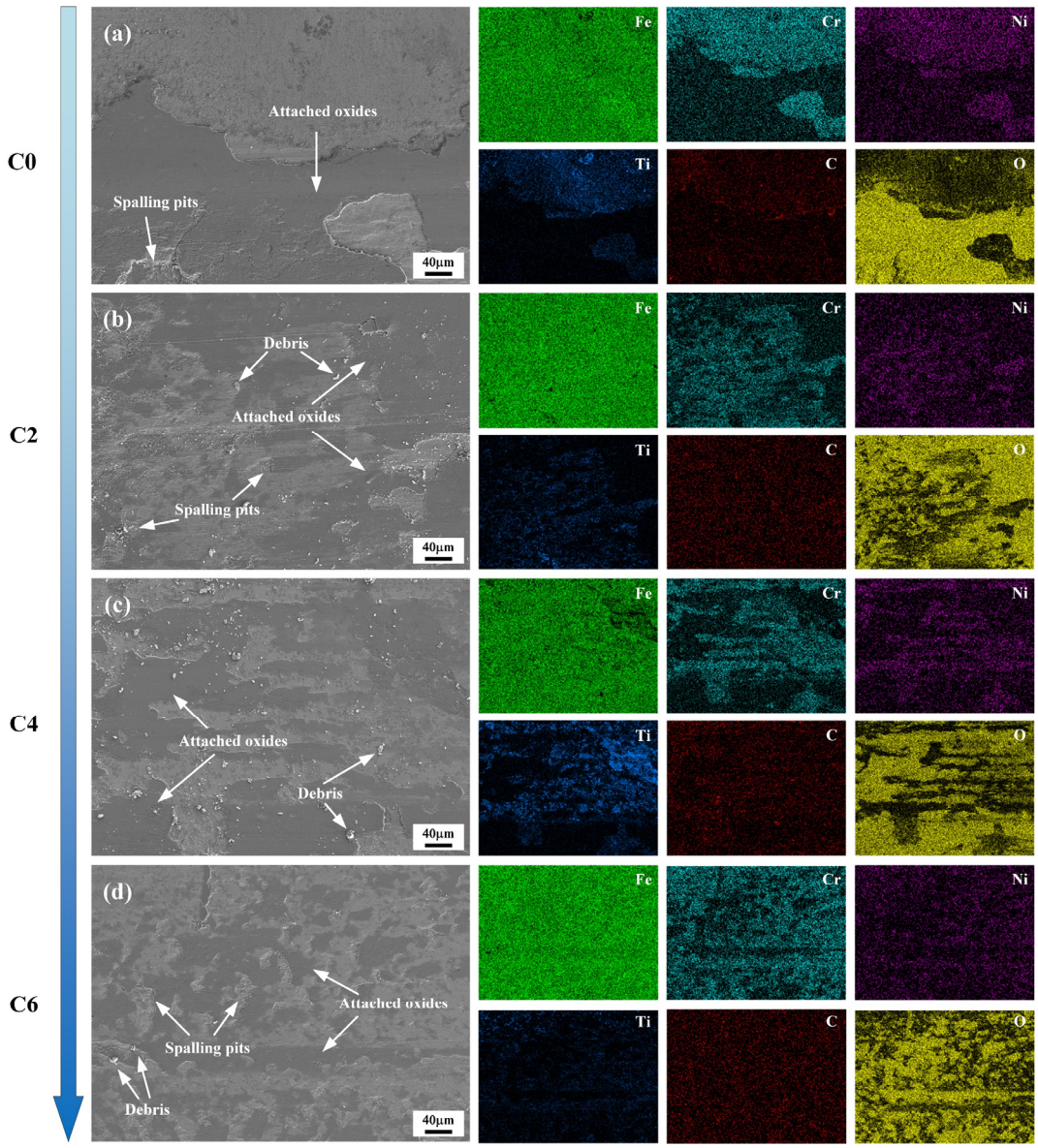

Figure 9. The wear morphology and element distribution on the C0 to C6 coating surfaces. (**a**) C0; (**b**) C2; (**c**) C4; (**d**) C6.

Point scanning was conducted on the wear morphology of the C4 coating, and the resulting element spectra are presented in Figure 10. Point 1 consists primarily of Fe and O elements, indicating that the oxide layer region is mainly composed of iron oxide. Point 2 is mainly composed of Fe elements and also contains Cr, Ni, Ti, C, and O elements, which indicates that there is a slight oxidation phenomenon on the surface of the coating. Point 3 is mainly composed of Ti, C, and O elements, leading to the conclusion that the wear debris primarily consists of titanium carbide particles and titanium oxide particles. This phenomenon arises because friction converts mechanical energy into thermal energy during the wear process, causing a significant temperature rise in the contact area. Titanium carbide then reacts with oxygen under high-temperature conditions to form titanium oxide. Given that titanium carbide and titanium oxide have much higher hardnesses than the coating, they are resistant to plastic deformation during wear and remain attached to the worn surface in the form of abrasive particles.

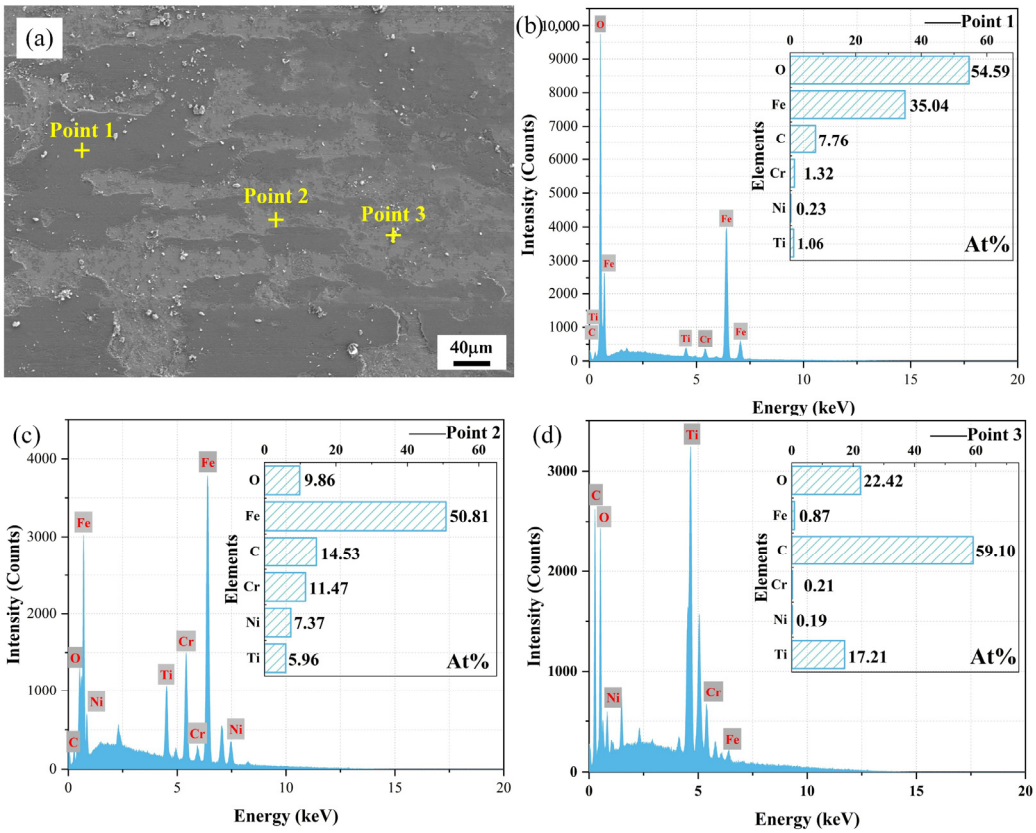

Figure 10. Point scanning results of C4 coating wear surface. (**a**) SEM results of the C4 coating; (**b**) point scanning result of point 1; (**c**) point scanning result of point 2; (**d**) point scanning result of point 3.

4. Conclusions

In this study, laser cladding technology was employed to fabricate 316 stainless steel + TiC coatings with different LaB_6 contents (0%, 2%, 4%, and 6%) on 45 steel surfaces. The effects of the LaB_6 content on the phase composition, microstructure evolution, Vickers hardness, and wear resistance of 316 stainless steel/TiC coatings were evaluated, and the wear mechanism of the coating was analyzed.

The phase composition of the coating without LaB_6 (C0) was composed of Austenite and TiC phases. With the increase in the LaB_6 content, Fe-Cr phases were generated in the coating, and the diffraction intensity of the Austenite phase decreased gradually. The microhardness of the coatings first increased and then decreased with the increase in the LaB_6 content. The C4 coating achieved the highest microhardness ($594HV_{0.2}$) due to the combined action of the grain refinement strengthening and TiC dispersion strengthening.

The tribological test results indicated that the wear rate of the coatings showed the same trend as the microhardness. The C4 coating exhibits the lowest wear rate and the best wear resistance. This is because its relatively high hardness enhances the resistance to plastic deformation and fatigue spalling, while the TiC particles play a “pinning role” that prevents the plowing effect of abrasive particles.

Author Contributions: Conceptualization, D.Z. and H.L.; Investigation, H.L., Y.L., and Y.G.; Resources, D.Z. and Y.L.; Data Curation, H.L. and J.J.; Writing—Original Draft Preparation, H.L.; Writing—Review and Editing, D.Z. and J.J.; Supervision, D.Z., Y.G., and Y.L.; Funding, D.Z. All authors have read and agreed to the published version of the manuscript.

Funding: This research was funded by the Department of Education of Jilin Province within the scope of the project numbered JJKH20250860KJ.

Institutional Review Board Statement: Not applicable.

Informed Consent Statement: Not applicable.

Data Availability Statement: The data that support the findings of this study are available from the corresponding author upon reasonable request.

Conflicts of Interest: The authors declare no conflicts of interest.

References

1. Chen, Y.B.; Zhou, J.Z.; Li, P.F.; Huo, K.; Meng, X.K. Effect of Electromagnetic Field on Wear Resistance of Fe901/Al_2O_3 Metal Matrix Composite Coating Prepared by Laser Cladding. *Materials* **2022**, *15*, 1531. [CrossRef]
2. Hu, Z.W.; Li, W.G.; Zhao, Y.T. The Effect of Laser Power on the Properties of M_3B_2-Type Boride-Based Cermet Coatings Prepared by Laser Cladding Synthesis. *Materials* **2020**, *13*, 1867. [CrossRef]
3. Zhang, Z.Q.; Niu, W.; Lei, Y.W.; Zheng, Y. The Effect of SiC Content on the Microstructure and Mechanical Properties of AlCoCrFeNiTi Laser Cladding High-Entropy Alloy Coatings. *J. Therm. Spray Technol.* **2025**, *34*, 1195–1207. [CrossRef]
4. Liu, Q.S.; Liu, X.B.; Wang, G.; Liu, Y.F.; Meng, Y.; Zhang, S.H. Effect of Cu content on microstructure evolution and tribological behaviors of Ni60 composite coatings on 45# steel by laser cladding. *Opt. Laser Technol.* **2022**, *156*, 14. [CrossRef]
5. Chen, W.J.; Yang, X.C.; Li, X.M.; Chai, C.; Liu, W.B. Study on Microstructure and Properties of Nickel-Based Self-Lubricating Coating by Laser Cladding. *Coatings* **2022**, *12*, 753. [CrossRef]
6. Chen, L.Y.; Chen, Y.; Chen, X.; Yu, T.B.; Wang, Z.X. Microstructure and properties of in situ TiC/Ni functionally gradient coatings by powder-fed laser cladding. *Ceram. Int.* **2022**, *48*, 36789–36801. [CrossRef]
7. Li, Y.J.; Dong, S.Y.; Yan, S.X.; Liu, X.T.; He, P.; Xu, B.S. Surface remanufacturing of ductile cast iron by laser cladding Ni-Cu alloy coatings. *Surf. Coat. Technol.* **2018**, *347*, 20–28. [CrossRef]
8. Wu, Q.L.; Li, W.G.; Zhong, N.; Gang, W.; Wang, H.S. Microstructure and wear behavior of laser cladding VC-Cr_7C_3 ceramic coating on steel substrate. *Mater. Des.* **2013**, *49*, 10–18. [CrossRef]
9. Jia, D.H.; Shi, W.Q.; Zhang, H.; Wu, T.; Diao, Y.L.; Li, K.Y.; Lu, C. Effects of Y_2O_3 Content on Wear Resistance and Corrosion Resistance of 316L/TiC Coating Fabricated by Laser Cladding. *Coatings* **2023**, *13*, 1348. [CrossRef]
10. Ge, H.H.; Ding, S.J.; Zhang, P.Z.; Fang, H.; Hu, Y.; Yao, J.H. Influence of overlapping process on the distribution of Cr element in laser cladding 316L powder on 45# steel substrate. *Surf. Coat. Technol.* **2024**, *493*, 12. [CrossRef]
11. Liu, Y.H.; Li, J.; Xuan, F.Z. Fabrication of TiC reinforced Ni based coating by laser cladding. *Surf. Eng.* **2012**, *28*, 560–563. [CrossRef]
12. Li, D.M.; Sun, X.F.; Li, Z.M.; Wei, S.; Zhao, H.X.; Peng, S.; Zheng, B.J. Effect of TiC content on the microstructure and properties of large-area laser-cladded TiC Ni-based composite coatings. *Mater. Res. Express* **2021**, *8*, 11. [CrossRef]
13. He, X.; Song, R.G.; Kong, D.J. Effects of TiC on the microstructure and properties of TiC/TiAl composite coating prepared by laser cladding. *Opt. Laser Technol.* **2019**, *112*, 339–348. [CrossRef]
14. Bu, R.; Jin, A.X.; Sun, Q.; Zan, W.; He, R.L. Study on laser cladding and properties of AZ63-Er alloy for automobile engine. *J. Mater. Res. Technol.* **2020**, *9*, 5154–5160. [CrossRef]
15. Xu, S.Y.; Cai, Q.; Li, G.; Lu, X.F.; Zhu, X.L. Effect of scanning speed on microstructure and properties of TiC/Ni60 composite coatings on Ti6Al4V alloy by laser cladding. *Opt. Laser Technol.* **2022**, *154*, 12. [CrossRef]
16. Wu, Q.L.; Long, W.M.; Zhang, L.; Zhao, H.W. A review on ceramic coatings prepared by laser cladding technology. *Opt. Laser Technol.* **2024**, *176*, 25. [CrossRef]
17. Li, G.S.; Wang, Z.Y.; Yao, L.G.; Xie, D.Z.; Chen, G. Concentration mixing and melt pool solidification behavior during the magnetic field assisted laser cladding of Fe-Cr-based alloy on 45 steel surface. *Surf. Coat. Technol.* **2022**, *445*, 16. [CrossRef]
18. Tao, L.; Yang, Y.; Zhu, W.L.; Sun, J.; Wu, J.L.; Xu, H.; Yan, L.; Yang, A.H.; Xu, Z.L. Stress Distribution in Wear Analysis of Nano-Y_2O_3 Dispersion Strengthened Ni-Based μm-WC Composite Material Laser Coating. *Materials* **2024**, *17*, 121. [CrossRef] [PubMed]
19. Xie, Y.J.; Jiang, W.Y.; Xu, K.G.; Wen, X.; Huang, B.S. Microhardness, wear resistance, and corrosion resistance of AlCoCrFe $Ni_{2.1}$+xCeO_2 high-entropy alloy coatings by laser cladding. *Mater. Today Commun.* **2025**, *43*, 14. [CrossRef]
20. Meng, L.Y.; Hu, M.; Zhao, H.Q.; Lv, P.; Wang, A.M. Influence of Nano Rare-Earth Oxides on the Microstructure and Wear Resistance of Laser Clad Micro-nanostructure Al_2O_3-NiCr Coating. *J. Mater. Eng. Perform.* **2025**, 12. [CrossRef]
21. Mohammed, S.; Rajamure, R.S.; Zhang, Z.; Balu, P.; Dahotre, N.B.; Kovacevic, R. Tailoring corrosion resistance of laser-cladded Ni/WC surface by adding rare earth elements. *Int. J. Adv. Manuf. Technol.* **2018**, *97*, 4043–4054. [CrossRef]
22. Li, Z.Y.; Chen, W.A.; Li, D.Y.; Yang, J.W.; Zhang, Y.; Yang, X.D.; Dai, B.G.; Zhang, J.H.; Qiu, Z.L. Frictional wear properties of different nano La_2O_3 composite FeCoNiCrMo high-entropy alloy coatings under soil conditions. *J. Mater. Res. Technol.* **2025**, *35*, 6874–6888. [CrossRef]

23. Wang, L.-M.; Lin, Q.; Yue, L.-J.; Liu, L.; Guo, F.; Wang, F.-M. Study of application of rare earth elements in advanced low alloy steels. *J. Alloys Compd.* **2007**, *451*, 534–537. [CrossRef]
24. Nie, M.H.; Zhang, S.; Wang, Z.Y.; Zhang, C.H.; Chen, H.T.; Chen, J. Effect of laser power on microstructure and interfacial bonding strength of laser cladding 17-4PH stainless steel coatings. *Mater. Chem. Phys.* **2022**, *275*, 125236. [CrossRef]